

Conductive n-type gallium nitride thin films prepared by sputter deposition

Cite as: J. Vac. Sci. Technol. A 40, 042703 (2022); doi: 10.1116/6.0001623

Submitted: 12 November 2021 · Accepted: 23 May 2022 ·

Published Online: 14 June 2022



Patrick Loretz,^{1,a)} Thomas Tschirky,¹ Fabio Isa,¹ Jörg Patscheider,¹ Matthias Trottmann,² Adrian Wichser,² Jacopo Pedrini,³ Emiliano Bonera,³ Fabio Pezzoli,³ and Dominik Jaeger¹

AFFILIATIONS

¹Evatec AG, Hauptstrasse 1a, 9477 Trübbach, Switzerland

²Swiss Federal Laboratories for Materials Science and Technology, Überlandstrasse 129, 8600 Dübendorf, Switzerland

³L-NESS and Dipartimento di Scienza dei Materiali Università degli Studi di Milano Bicocca, via Roberto Cozzi 55, 20125 Milano, Italy

Note: This paper is a part of the Special Topic Collection on Functional Coatings.

a) Author to whom correspondence should be addressed: Patrick.Loretz@evatecnet.com

ABSTRACT

Given the recent increase in the demand for gallium nitride (GaN) in different markets like optoelectronics and power devices, the request for epitaxially grown GaN will further increase. To meet this high demand, higher throughput and more economical manufacturing technologies must be advanced. In this work, GaN thin films are deposited by reactive sputter deposition from a liquid gallium target at a substrate temperature of 900 °C. The layers are grown epitaxially on c-plane oriented sapphire in an industrial-scale sputter tool from Evatec AG. Due to the growth rate of >1 nm/s and the fast substrate heat-up time, the throughput in a production setup can be increased compared to other GaN growth techniques. The resistivity of the intrinsic insulating GaN can be lowered by intentional Si doping during the sputter deposition process by three orders of magnitude. Thereby, conductive n-type GaN can be grown with different dopant amounts. The carrier mobility of the sputter deposited film is $45 \text{ cm}^2 \text{ V}^{-1} \text{ s}^{-1}$ at a carrier concentration of $1.1 \times 10^{20} \text{ cm}^{-3}$ based on room temperature Hall measurements using a van der Pauw geometry. The lowest resistivity reaches $1300 \mu\Omega \text{ cm}$, which is confirmed by sheet resistance measurements. Undoped films exhibit an x-ray diffraction rocking curve full width at half maximum of 0.2° , which increases up to 0.5° for highly Si-doped layers. The presented results show that GaN prepared by reactive sputter deposition from a liquid gallium source is a viable alternative to conventional deposition techniques for GaN.

Published under an exclusive license by the AVS. <https://doi.org/10.1116/6.0001623>

I. INTRODUCTION

The nitrides of group III elements in their wurtzite phase, notably indium nitride (InN), aluminum nitride (AlN), and gallium nitride (GaN), have attracted much attention due to their excellent optical and electrical properties for a wide field of technological applications. Especially, GaN is the subject of increasing economic interest because of its unique material properties. Particularly, high breakdown voltage, high carrier mobility, large direct bandgap of 3.4 eV, and the ability of substitutional doping to yield p-doping (e.g., with Mg) and n-doping (e.g., with Si) make this material highly suitable for light-emitting diodes (LEDs),^{1,2} lasers for communication applications,³ power transformer devices,^{4,5} as well as consumer electronics,⁶ and many more. As an

example, the applications of GaN-based laser diodes in vertical-cavity surface-emitting lasers⁷ may be mentioned, and a continuous increase in the demand of GaN-based products can be expected in the future.

The comparable lattice constants of the wurtzite group III-nitrides AlN, GaN, and InN enable their ternary and quaternary alloys to cover a bandgap energy range between 0.7 and 6.2 eV, thus allowing to tune the light emission between IR and UV.⁸

Since the successful production of blue LEDs in the 1990s,⁹ GaN has experienced an extreme increase in demand, predominantly in the fields of opto- and power electronics. Nowadays, GaN is an essential compound in commercial blue and UV LEDs. Increased energy efficiency in lighting applications required to

meet the goals of the Paris Agreement on climate change drives the demand for LED lighting. Moreover, the demand for UV disinfection lamps has been increasing steadily, now amplified by the recent COVID-19 pandemic,¹⁰ which can be realized by GaN-based LEDs.

To achieve the GaN properties required for high light output, the losses due to epitaxial defects must be minimized, thereby implying a nearly perfect crystal growth. Metal organic chemical vapor deposition (MOCVD)^{11,12} is the current method of choice for the large scale production of low defect density GaN films, whereas research on thin films is often performed with molecular beam epitaxy (MBE).¹³ Bulk GaN wafers having diameters of up to 4 in. can be produced efficiently using hydride vapor phase epitaxy (HVPE).^{14,15} Sputter deposition of epitaxial GaN has attracted considerable attention through the production of a highly crystalline AlN buffer layer with postannealing,^{16,17} while reactive sputter deposition is still in its early stages of development for GaN due to the low melting temperature of the metallic Ga target. The high throughput, good scalability, and relatively low cost of ownership make sputter deposition an attractive alternative for mass production. The absence of carbon, a frequently encountered contaminant in processes using organo-metallic compounds as in MOCVD, PECVD, and PEALD, is a further advantage of sputter deposited GaN films. In the last decade, the preparation of GaN by sputter deposition has, therefore, become a widely investigated field.^{18–22}

The deposition viability of highly crystalline GaN films by reactive sputtering from a liquid gallium target was shown by Junaid.²¹

For manufacturing devices based on GaN, the ability to control the resistivity by incorporating dopants in the layers to a high concentration and in a controlled manner is of paramount

importance. For n-type doping with Si, a carrier density of $5.1 \times 10^{20} \text{ cm}^{-3}$ and a carrier mobility of $100 \text{ cm}^2 \text{ V}^{-1} \text{ s}^{-1}$ have been achieved with pulsed sputter deposition by Arakawa *et al.*²³

This work explores the feasibility of doping GaN by Si cosputtering as a dopant material.

We present a detailed study on the sputter deposition from the liquid Ga target and material characterization of Si-doped GaN layers exhibiting carrier densities ranging between 9×10^{17} and $1.1 \times 10^{20} \text{ cm}^{-3}$, and electron mobilities between 11 and $45 \text{ cm}^2 \text{ V}^{-1} \text{ s}^{-1}$, respectively.

II. EXPERIMENT

The GaN films are prepared in a Clusterline® 200II (Ref. 24) system manufactured by Evatec AG in a modified process module to accommodate the liquid gallium target material. Sputtering from a liquid target, as compared to a solid target, removes the need for a high-capacity cooling system and makes high growth rates possible as well as easier scaling to larger substrate sizes. A controlled temperature system keeps the target above the melting point (ca. 30 °C), as depicted in the schematic drawing of the sputter process module in Fig. 1. The 2 in. sapphire substrates are placed on a 6 in. fused silica carrier and transferred to the deposition module. The substrates, placed on IR-absorbing fused silica, are heated radiatively from the backside by a carbon heater to a maximum temperature of 900 °C. Temperature calibration has been performed beforehand using thermocouples attached to a silicon wafer. Except for a bakeout step in the module, the sapphire substrates are not precleaned. The transfer system places the substrate 75 mm away from the target. Metal shielding protects the chamber from unintentional coating and confines the plasma laterally to the gallium target. Using a turbomolecular pump, a base pressure

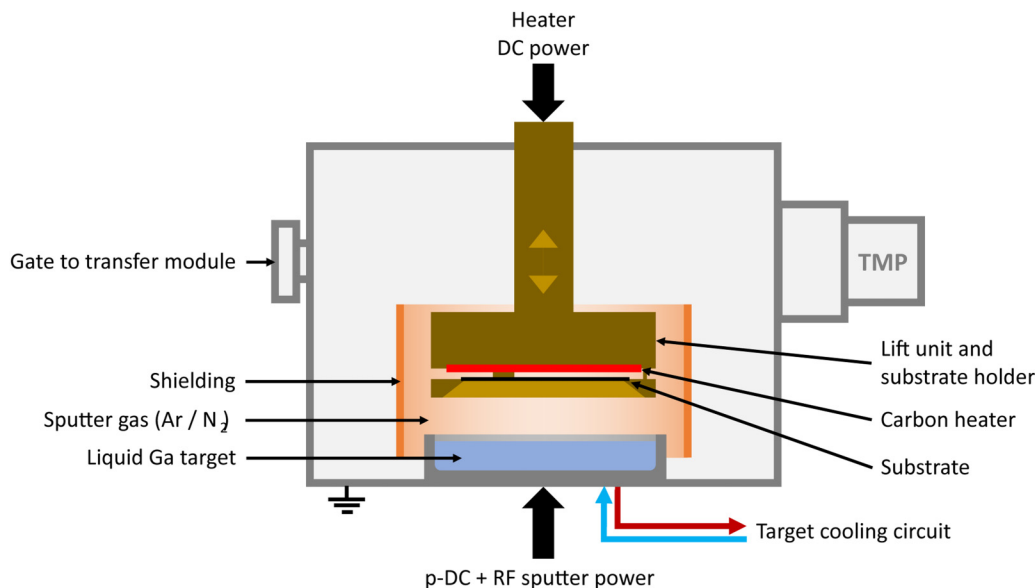


FIG. 1. Schematic drawing of the sputter process module. The main components are the liquid Ga target, the carbon heater, and the shielding.

TABLE I. List of process parameters used for the deposition of the GaN samples analyzed in this paper. The optimization range (min–max value) is indicated for each process parameter, among which the deposition parameters were selected to produce 1 μm thick GaN films.

Process parameter	Deposition parameter	Optimization range
p-DC power (W)	73	0–1500
Duty-cycle (%)	64	64–100
RF power (W)	242	0–1500
RF frequency (MHz)	13.56	13.56/40.68
Temperature ($^{\circ}\text{C}$)	900	500–900
Pressure (mbar)	2.0×10^{-3}	8.4×10^{-4} – 6.3×10^{-3}
Target-substrate distance (mm)	70	60–90
Ar/N ₂	0.78	0.05–0.78

of $< 2 \times 10^{-8}$ mbar is reached. By introducing the process gases, Ar and N₂ (5N quality), the pressure is adjusted to 3×10^{-3} mbar. The sputter power is delivered by a 300 W pulsed DC (p-DC) generator with a frequency of 300 kHz and a duty-cycle of 64%, which is superimposed to 1000 W RF at 13.56 MHz frequency. These deposition parameters (summarized in Table I) have been selected by previous experiments, where each parameter was varied within a certain optimization range (see also Table I), producing 1 μm thick GaN films with a deposition rate of 1 nm/s and an XRD 002 rocking curve (RC) FWHM $\leq 0.35^{\circ}$.

During the sputter process, the Lorentz forces induced by the plasma current and the magnetic field cause the liquid target material to move in a manner that prevents the formation of gas

bubbles and thus avoids the ejection of target material droplets toward the substrate;²⁵ an unwanted effect already reported by Junaid.²¹

Si doping is achieved by placing a silicon wafer bar off-center above the gallium target to generate a concentration gradient on the substrate (see Fig. 2). With this arrangement, different Si doping concentrations originating from the same sputter process can be obtained and evaluated for each 2 in. GaN/sapphire sample.

Indeed, 2 in. sapphire substrates are positioned on a 6 in. carrier, on which GaN:Si was deposited. The substrates are placed at different distances to the Si bar, as shown in Fig. 1, thereby resulting in GaN films with different doping concentrations. The undoped sample (sample A) is positioned arbitrarily on the 6 in. carrier in the absence of the Si doping bar. Sample B has the Si doping bar placed close to the edge of the target as depicted in Fig. 2(a). In this arrangement, the Si bar is tangent to the outer edge of the plasma racetrack, which is confined at the dashed line that also indicates the rim of the 6 in. carrier. For samples C to E [Fig. 2(b)], the doping bar is placed further away from the target edge and within the high intense plasma. Sample C is placed furthest away from the doping bar, sample D is placed at a medium distance, and sample E closest to the Si doping bar. Figures 2(c) and 2(d) illustrate the distance of the Si doping bar to the edge of the Ga container in a cross-sectional view.

The GaN layers are characterized with respect to surface topography, crystallinity, as well as for their optical and electrical properties. Furthermore, elemental analysis is performed by laser ablation inductively coupled plasma mass spectrometry (LA-ICP-MS) to estimate the concentration of the dopant.

LA-ICP-MS is a technique for determining trace elements in solids, and its quantitative analysis requires calibration standards,

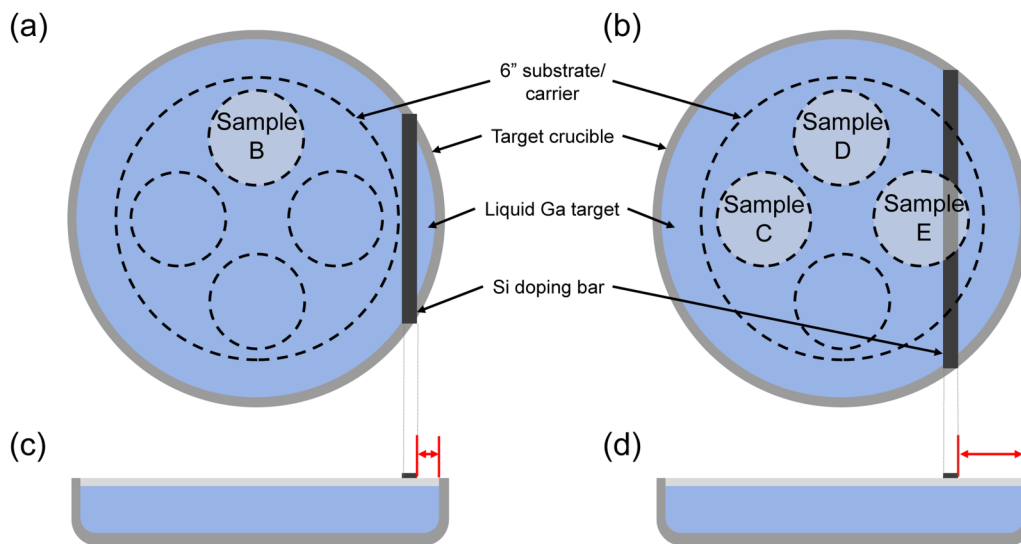


FIG. 2. Schematic drawing of the target crucible containing the liquid target material. The doping silicon bar is placed on top of the crucible; the dotted line indicates the rim of the 6 in. carrier. (a) Top view of sample B setup, (b) setup of samples C–E. (c) and (d) are the side views, where the distance of the Si bar to the target edge is indicated.

which, however, are not available for this work. A Nd:YAG laser with a wavelength of 532 nm is used to ablate an area of 500 μm in diameter with a single 5 mJ laser pulse. To collect enough material for sufficient statistics, the entire GaN layer thickness is ablated with 10 laser pulses, and 5 measurements are made per sample. The ablated material is ionized by an inductively coupled plasma and analyzed in a Nexion 2000 mass spectrometer from Perkin Elmer. The reported doping is determined from the ^{29}Si isotope intensity integrated over the measurement time after background intensity subtraction.

The surface roughness and topography are characterized by atomic force microscopy (AFM) on a Park Systems NX20 in a non-contact mode with a resolution of 512×512 pixels over an area of $5 \times 5 \mu\text{m}^2$. Scanning electron microscopy (SEM) with a FEI Quanta 200F microscope is performed with 10 kV at a high pressure (60 Pa) to suppress charging effects of the insulating GaN material. The SEM images are recorded at a scale of 30 μm .

The crystallinity is analyzed using a Bruker D8 Discover x-ray diffractometer (XRD) equipped with a Göbel mirror and a $2 \times$ Ge monochromator on the primary beam axis and a compound silicon strip detector in a 0D mode. $\theta/2\theta$ scans and rocking curves (RCs) (ω -scans) are performed on the basal (002) and the asymmetric (102) planes. Additionally, higher order diffraction peaks (002, 004, and 006) for the Williamson–Hall (W–H) analysis method are measured.

Raman spectroscopy is performed using a confocal Horiba LabRAM HR Evolution tool equipped with a 532 nm laser and 100×0.9 NA objective (0.5 cm^{-1} spectral resolution) measuring the GaN samples in line scans of ten points separated by 1 μm each. The laser power and acquisition time range from 1 to 1.2 mW and 15–30 s, respectively. At every position, the Raman spectrum is acquired between 400 and 800 cm^{-1} in the $Z(X-\bar{Z})$ configuration according to the Porto notation $A(BC)D$, where A is the excitation (laser) propagation direction, B is the excitation (laser) polarization direction, C (if present) is the Raman scattering polarization

direction, and D is the Raman scattering propagation direction. In our setup, Z and X were parallel to the [001] and $[2\bar{1}0]$ GaN crystal directions, respectively.

Photoluminescence (PL) measurements are acquired with the same setup used for Raman spectroscopy. The excitation energy is 5.0 eV coming from a frequency-doubled continuum laser with emission at 244 nm operating at an intensity of about 10 mW. The illumination radiation is focused by a 0.40 NA objective working in the UV spectral range. The same objective collects light in the backscattering configuration and sends the light into the spectrometer with better than 1 nm bandpass resolution.

The GaN electrical properties are investigated by a Four Dimensions Four Point Probe (4PP) resistance measurement tool with a maximum recordable sheet resistance of 800 k Ω /sq. The carrier concentration and carrier mobility are determined using a rectangular van-der-Pauw sample geometry on a Hall measurement setup at room temperature. The $5 \times 5 \text{ mm}^2$ samples are contacted by soldering gold wires to the edges and corners of the sample using indium as the solder. A perpendicular magnetic field of 0.5 T is applied by water-cooled magnets and a measurement current of 0.1 mA applied in both edge and corner contact configurations. Each sample is measured three times in each configuration and the standard deviation error is calculated. An additional magneto-transport measurement with 100 points between 0 and 1 T is performed to check the linear increase of the Hall resistance with the B-field.

III. RESULTS AND DISCUSSION

For reference purposes, undoped GaN samples (sample A) have been characterized. The Si content, determined by LA-ICP-MS beforehand, is at the quantification limit with an integrated intensity of 185 ± 146 (Fig. 3). The resistivity is above the instrument limit; hence, it could not be determined by 4PP nor Hall measurement. The crystal properties, determined by XRD, show a high crystallinity with a 002 FWHM of 0.23° [Fig. 10(a)]. Only 002 or higher orders of diffraction are seen in the $\theta/2\theta$ plot shown in Fig. 7, demonstrating oriented growth. The screw and mixed dislocation density (DD) determined by the Williamson–Hall method from symmetric XRD reflections²⁶ is $1.0 \times 10^9 \text{ cm}^{-2}$, while the surface topography shows pronounced hillocks (not shown) on the surface and a surface roughness R_q of 48 nm. The Raman spectrum shows only the $E_2^{(2)}$ mode and a peak at the $A_1(\text{LO})$ mode as shown in Fig. 11 and will be discussed later.

Table II gives a summary of the most relevant properties of samples A–E.

Samples B to E are intentionally doped with Si, which is confirmed by the LA-ICP-MS. The Si doping concentrations of the different samples are plotted in Fig. 3. The curves show a small signal intensity for sample B with an integrated intensity of 753 ± 99 (a.u.). Samples C and D have a slightly higher signal intensity of 736 ± 212 (a.u.) and 1085 ± 136 (a.u.). The sample with the highest doping is sample E with an intensity of 3617 ± 103 (a.u.). The inset picture shows the integrated intensities of samples A to E.

In Fig. 4, the ^{29}Si concentration of the Si-doped samples is plotted versus the carrier concentration and the resistivity. By measuring the resistivity, the influence of doping becomes more apparent. Undoped GaN has a resistivity above the instrument limit;

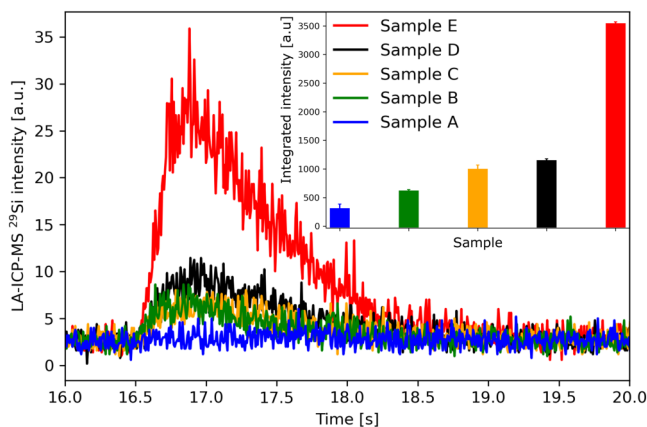


FIG. 3. LA-ICP-MS signal for the ^{29}Si isotope of sample A (blue), B (green), C (orange), D (black), and E (red). The inset shows the integrated intensity of the LA-ICP-MS signal for the ^{29}Si isotope for samples A–E. This figure's color version is available online.

therefore, no results could be obtained from the Hall measurement, which show the highly insulating property of sputter deposited GaN. Once Si as the doping material is added to the sputter process, the resistivity of the films is reduced. The higher the doping amount in the GaN layer, the lower the resistivity becomes, while the resistivity is lowered by more than three decades from 3×10^6 to $1.3 \times 10^3 \mu\Omega \text{ cm}$.

Figure 4 shows that increasing the doping concentration leads to a higher carrier concentration. The reduced resistivity is mainly caused by the higher carrier concentration [$n_e = 1/(qR_H)$ with q is the elementary charge and R_H is the Hall coefficient] for increased Si concentrations. Due to increasing doping, the carrier concentration rises from $9.5 \times 10^{16} \text{ cm}^{-3}$ for sample B to $1.1 \times 10^{20} \text{ cm}^{-3}$ for sample E. The steep increase in the charge carrier concentration for the lower concentration can be explained by the trapping of charges at dislocation lines, as described in Ref. 27. The highest amount of doping shows that the additional Si is still active as an n-type dopant and does not self-compensate or segregate significantly.

The carrier mobility [$\mu = 1/(qn_e\rho_{xx})$ with ρ_{xx} being the longitudinal resistance], as determined by Hall measurements, changes only slightly over the carrier concentration range, as shown in Fig. 5. The carrier mobility for sample B and sample C amounts to $23 \pm 5.3 \text{ cm}^2 \text{ V}^{-1} \text{ s}^{-1}$ and $11 \pm 1.7 \text{ cm}^2 \text{ V}^{-1} \text{ s}^{-1}$, respectively. For the higher doped GaN films, the carrier mobility increases to $40 \pm 2.0 \text{ cm}^2 \text{ V}^{-1} \text{ s}^{-1}$ (sample D) and $45 \pm 3.8 \text{ cm}^2 \text{ V}^{-1} \text{ s}^{-1}$ (sample E), respectively. This indicates that the ionized impurities introduced by Si-doping are not the sole scattering source for these layers in the studied concentrations. Most likely carrier scattering at dislocation lines, intrinsic point defects, grain boundaries, and extrinsic atomic impurities contribute significantly to the overall low carrier mobilities.²⁸ The increased mobility in the highly doped samples is a result of the changes in morphology and crystal growth in those samples²⁷ (Fig. 6).

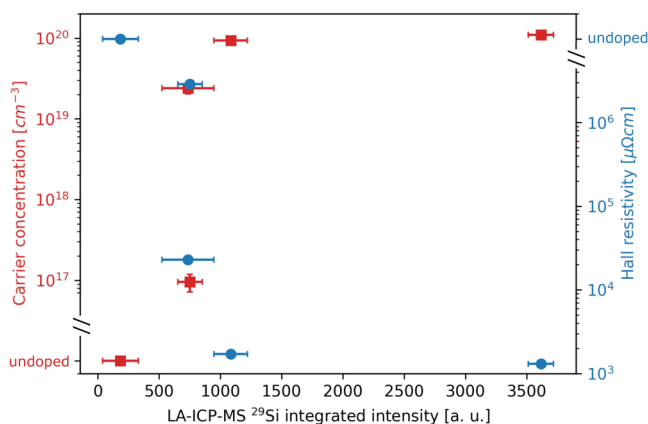


FIG. 4. Carrier concentration of the Si-doped samples (red squares) compared to the Hall resistivity (blue circles) as a function of the ²⁹Si integrated intensity measured by LA-ICP-MS. The carrier concentration increases with increasing doping concentration. The resistivity is reduced with increasing doping concentration. This figure's color version is available online.

The surface morphology varies with the doping concentration, as shown in Fig. 6 by the AFM and SEM images on different size scales. For the undoped (sample A) and very low doping concentration (sample B), the surface constitutes of pronounced hillocks with rounded edges [Figs. 6(a) and 6(b)], resulting in a surface roughness R_q of 48 and 41 nm, respectively. The formation of these hillocks is attributed to an uphill mass-current of adatoms generated by an Ehrlich-Schwöbel barrier.²⁹ By increasing the doping concentration, the hillocks become wider and taller with sharper edges, as shown for sample C in Fig. 6(c). Upon further increasing the doping concentration (sample D), the surface morphology changes, and the growth of flat islands occurs next to hillocks, as indicated by the dashed black ellipse in Fig. 6(d). For the highest Si doping concentration sample E, the surface exhibits a considerably flattened morphology without hillocks and a roughness R_q of 18 nm, as reported in Fig. 6(e). The edges of these structures indicate step-bunching, as the flanks are nearly vertical and can be several nm tall. We attribute this change in morphology, at least partially, to the effect of high fluxes of Si as a surfactant in GaN growth, thereby altering the surface kinetics. This effect was found by Mula *et al.*³⁰ to be even stronger with Mg as a dopant, which is confirmed by our preliminary experiments exhibiting the same changes in morphology (not shown here). The SEM images reported in Figs. 6(f)–6(j) confirm that the surface properties measured by AFM and previously described are uniform over the entire wafer surface.

To check whether a different morphology alters the orientation of the layers, $\theta/2\theta$ diffraction scans are performed. In Fig. 7, $\theta/2\theta$ scans are plotted for samples A to E, where only crystal planes parallel to the sample surface are visible. The 002 diffraction peak is shown in the image inset, and a shift of the 2 θ peaks for the samples is visible. The peak intensity decreases with increasing doping concentration.

The variation of Si doping has a pronounced impact on the crystallinity of the GaN layers. Figure 8 shows the normalized rocking curves (RCs) of the 002 (a) and 102 (b) peaks, where the

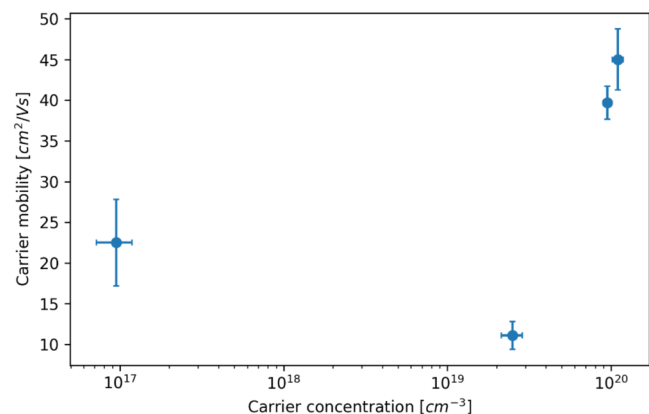


FIG. 5. GaN carrier mobility as a function of the carrier concentration.

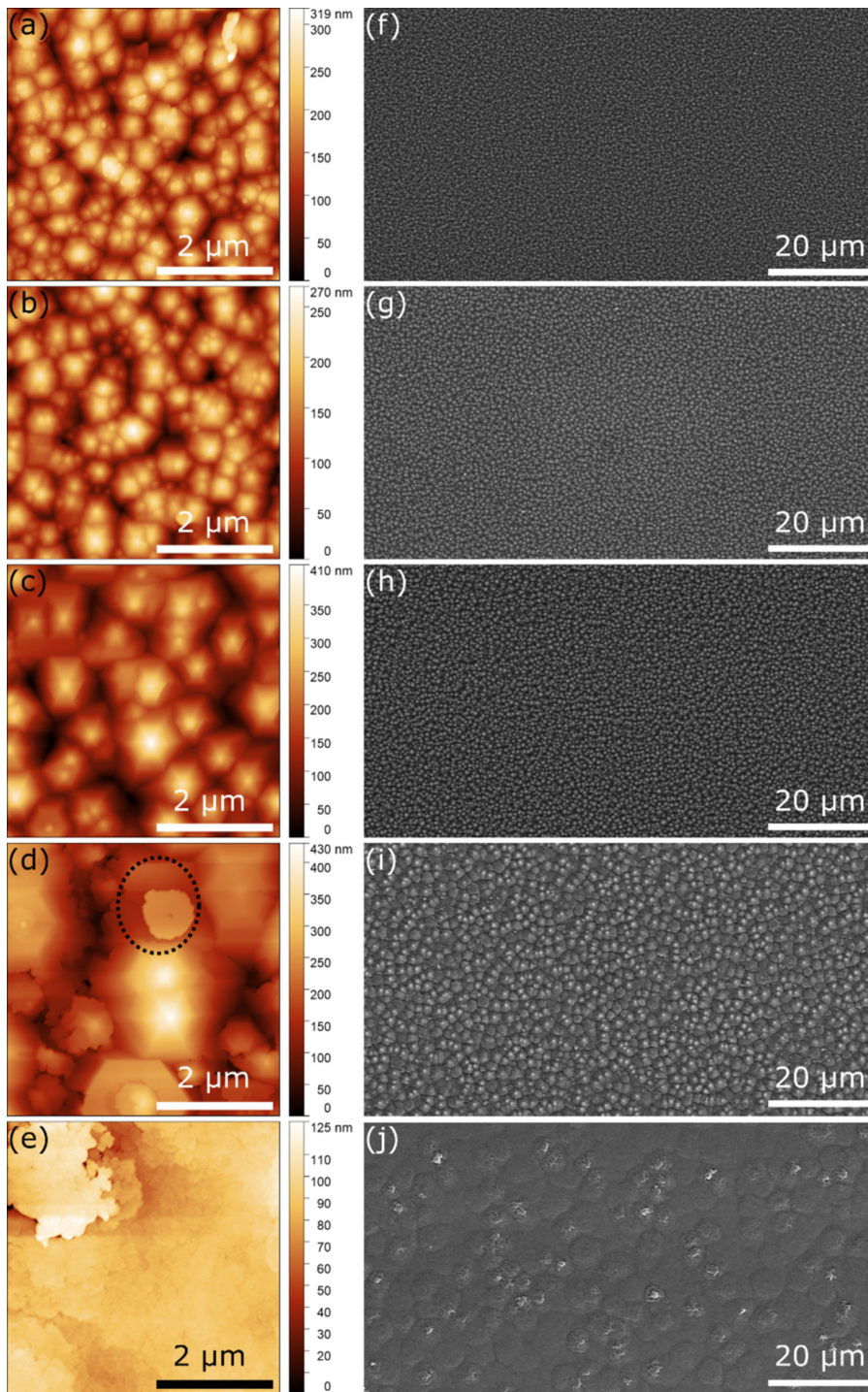


FIG. 6. (a)–(e) AFM surface topography images of the GaN layers with different Si doping. (a) GaN sample A, (b) GaN sample B, (c) GaN sample C, (d) GaN sample D, and (e) GaN sample E. The x–y dimensions of the GaN films are indicated by the size-bar, while the z-height morphology is displayed by the color scale. In (d), the dashed black ellipse indicates a GaN flatter area compared to the surrounding hillocks. (f)–(j) larger scale SEM images of the same GaN layers reported in (a)–(e), respectively.

broadening of sample E becomes apparent. However, the intensity for the 102 reflection is much lower as for the 002.

The FWHM of the 002 RC is below 0.5° for all samples as shown in Fig. 10(a); for the best samples (A and C), the FWHM

are 0.23° and 0.21° , respectively. These results are similar, or even superior, compared to other GaN layers deposited by sputtering already present in the literature,^{31,32} confirming the GaN high crystal quality. For the higher doped samples (D and E), the

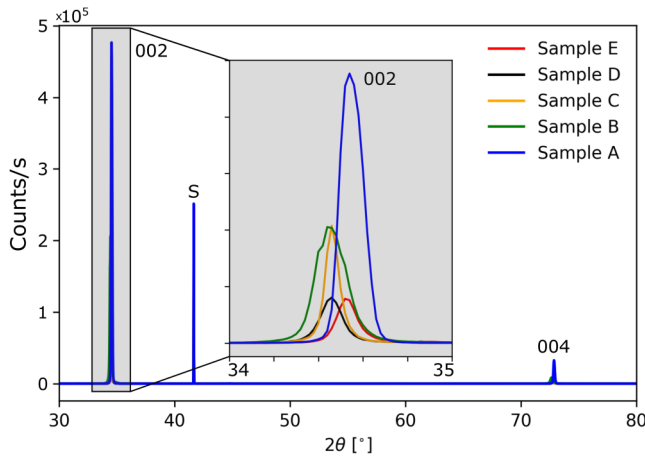


FIG. 7. XRD $\theta/2\theta$ scans of the GaN samples A–E. The 002 and 004 GaN XRD peaks are shown at around 34.5° and 72.7° , together with the 006 peak of the sapphire substrate (S). The gray inset shows a magnification of the XRD peaks for the different GaN samples between the 2θ angle of 34° and 35° .

FWHM are 0.42° and 0.49° , respectively. The FWHM of the 102 peaks exhibits the same trend but at slightly higher values than those of the 002 peaks. To further confirm the epitaxial relation of the GaN layers on sapphire (0001), an XRD intensity scan through the sample in-plane rotation angle ϕ ($0^\circ < \phi < 180^\circ$), while aligned on the asymmetric 102 GaN peak (Fig. 9), shows a clear sixfold

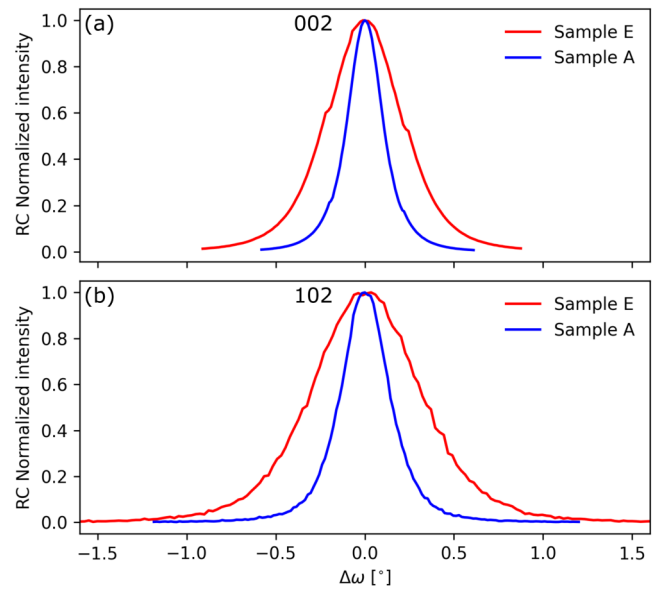


FIG. 8. (a) XRD rocking curves of the GaN sample A (blue line) and E (red line) for the 002 diffraction peak. (b) Same as (a) but for the 102 diffraction peak. The peaks are normalized in intensity and centered along ω for clarity. Discontinuities in (a) are due to x-ray attenuator changes. This figure's color version is available online.

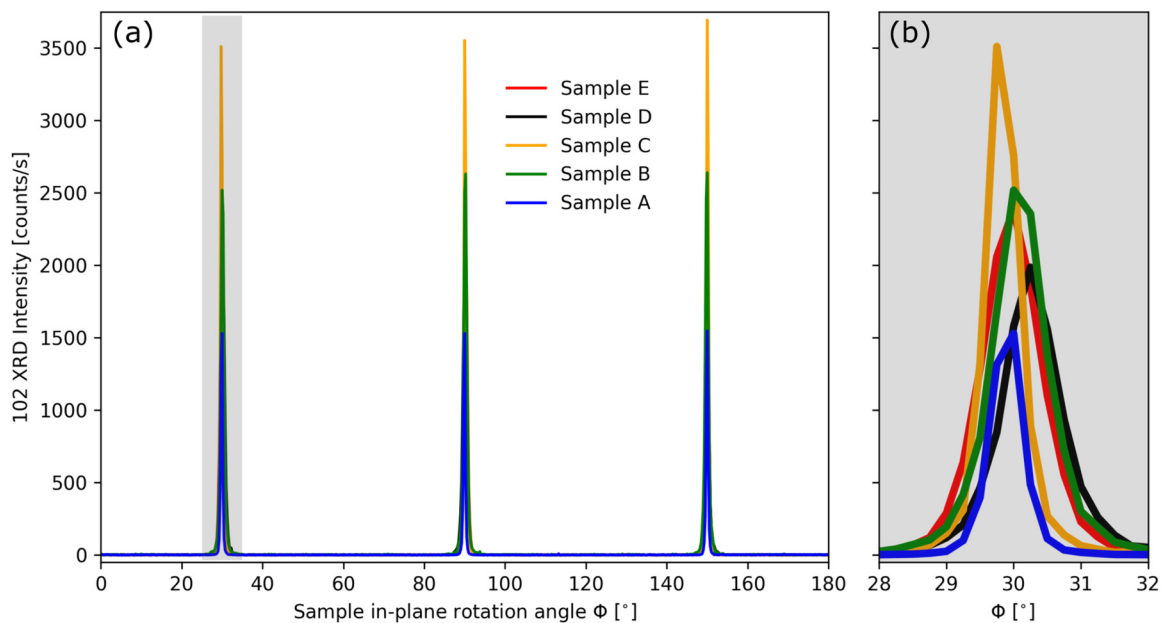


FIG. 9. (a) XRD scan through the sample in-plane rotation angle ϕ with diffraction conditions aligned on the 102 GaN peak for samples A–E. (b) Magnification of the XRD results reported in (a) between $28^\circ \leq \phi \leq 32^\circ$ marked by the gray rectangle.

symmetry with narrow diffraction peaks (FWHM along $\phi < 1^\circ$), indicating a highly uniform in-plane GaN orientation for samples A–E. As reported in Fig. 10(b), the center of the 002 $\theta/2\theta$ peak for the undoped GaN layer (sample A) slightly differs from the bulk GaN reference (blue star) with a value of 34.570° (Ref. 33). This indicates that the undoped GaN sample A is almost fully relaxed, as evidenced by the comparison with the bulk value indicated by the star. Doping with Si shifts the 2θ peak by 0.09° to lower angles, which translates to a compressive out-of-plane stress of -0.69 GPa (Ref. 34). Increasing the Si doping up to a carrier concentration of $9.5 \times 10^{19} \text{ cm}^{-3}$ (samples B–D), the values of the 002 $\theta/2\theta$ XRD peak center reduce to 34.462° , indicating an increase in the compressive stress within the GaN layer induced by the deformation of the crystal lattice due to the large amount of Si impurities. If the amount of Si impurities is further increased (sample E), the GaN layer relaxes the large amount of stress, and the center of the 002 $\theta/2\theta$ peak reaches the value of 34.536° , similar to the undoped sample A and bulk GaN reference. This trend is also observed on the surface morphology, where samples B to D exhibit pronounced hillock growth, while on sample E, an island growth morphology is observed. Additionally, the increase in the Si doping has a detrimental effect on the DD, which is calculated by the Williamson–Hall method²⁶ from the FWHM of the basal (002, 004, 006) diffraction peaks. Measurements on these peaks are only able to estimate the density of pure screw type and mixed type dislocations, whereas for determining the density of pure edge dislocations, measurements on asymmetric planes are required.³⁵ The comparison of 002 and 102 rocking curve FWHMs in Fig. 10(a) shows that the

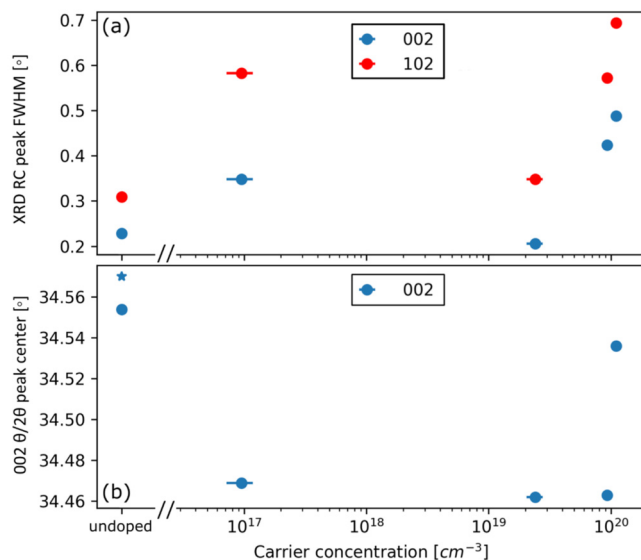


FIG. 10. GaN XRD results as a function of the carrier concentration. (a) FWHM of the RC 002 (blue circles) and 102 (red circles) GaN diffraction peaks as a function of the carrier concentration and (b) the 002 $\theta/2\theta$ peak center angle as a function of the carrier concentration. The blue star in (b) shows the calculated reference value of undoped, bulk GaN (Ref. 33). This figure's color version is available online.

layers contain a considerable amount of pure edge dislocations that, however, follows the same trend given by the pure screw and mixed dislocations. A minimum DD is reached for sample B, which also shows the largest hexagonally shaped hillocks. The screw and mixed DD for sample C is estimated to be lower than $3 \times 10^9 \text{ cm}^{-2}$, and the surface shows island next to hillock growth. For higher doping concentration (samples D and E), the screw and mixed DD increases to $7 \times 10^9 \text{ cm}^{-2}$, and the surface morphology shows no hillocks, only a step-bunchinglike growth with large islands.

Intensity-normalized Raman spectra of GaN with different amounts of Si doping are reported in Fig. 11 with the following carrier concentrations: sample A, undoped (blue), sample C with $2.5 \times 10^{19} \text{ cm}^{-3}$ (orange), sample D with $9.5 \times 10^{19} \text{ cm}^{-3}$ (gray), and sample E with $1.1 \times 10^{20} \text{ cm}^{-3}$ (yellow).

The main Raman spectral features consist of (1) a sharp Raman peak (S) at 417 cm^{-1} originating from the sapphire substrate, whose position does not change with Si doping levels. (2) Broad transversal optical $A_1(\text{TO})$ GaN phonon mode around 530 cm^{-1} , (3) $E_2^{(2)}$ GaN phonon mode around 568 cm^{-1} , and (4) longitudinal optical phonon modes: $A_1(\text{LO})$ and $E_1(\text{LO})$ at 735 and 743 cm^{-1} , respectively.^{36,37}

The intensity and spectral position of the GaN Raman peaks presented in Fig. 11 strongly depend on the Si doping concentration in the GaN layer. Three main effects are observed with the increase of Si dopant concentration: First, the appearance of the GaN $A_1(\text{TO})$ phonon mode, second the broadening and disappearance of the $A_1(\text{LO})$ phonon mode and appearance of the $E_1(\text{LO})$ phonon mode, and third the blue shift and broadening of the $E_2^{(2)}$ phonon mode.

The $A_1(\text{TO})$ Raman peak is absent for the undoped (blue line) and low doped $2.5 \times 10^{19} \text{ cm}^{-3}$ (orange line) GaN samples (A and C), while it appears for higher doping concentrations of $9.5 \times 10^{19} \text{ cm}^{-3}$ (sample D) and $1.1 \times 10^{20} \text{ cm}^{-3}$ (sample E).

The $A_1(\text{TO})$ Raman mode is forbidden for the $Z(X-\bar{Z})$ configuration in a perfect $Z//[001]$ GaN single crystal, while it is allowed for the $Z(Z-\bar{X})$ configuration.^{37–39} This result indicates

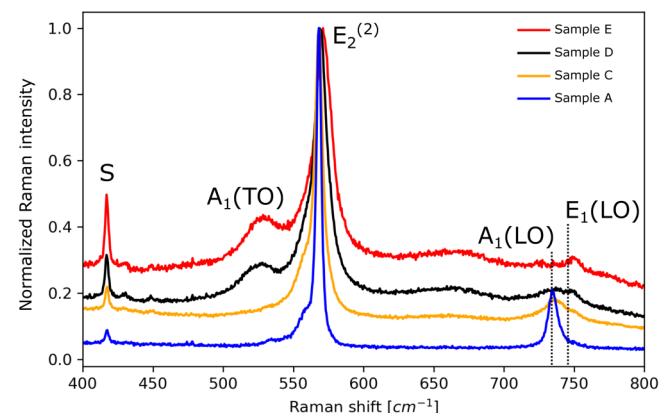


FIG. 11. Raman spectra of GaN layers on sapphire with different carrier concentrations: undoped (blue—sample A), $2.5 \times 10^{19} \text{ cm}^{-3}$ (orange—sample C), $9.5 \times 10^{19} \text{ cm}^{-3}$ (black—sample D) and $1.1 \times 10^{20} \text{ cm}^{-3}$ (red—sample E), recorded in the $Z(X-\bar{Z})$ configuration. $A_1(\text{TO})$, $E_2^{(2)}$, $A_1(\text{LO})$, and $E_1(\text{LO})$ indicate different GaN phonon modes, S indicates the sapphire Raman mode. This figure's color version is available online.

TABLE II. Sample overview with integrated intensity of the LA-ICP-MS measurement, the resistivity and the carrier concentration, and carrier mobility of the Hall measurement and dislocation densities.

	Integrated ^{29}Si intensity (a.u.)	Resistivity ($\mu\Omega\text{ cm}$)	Carrier concentration (cm^{-3})	Carrier mobility ($\text{cm}^2\text{ V}^{-1}\text{ s}^{-1}$)	Dislocation density (screw and mixed) (10^9 cm^{-2})
Sample A	185	N/A	N/A	N/A	1.0
Sample B	753	3×10^6	1×10^{17}	22.5	2.8
Sample C	736	2.3×10^4	2.4×10^{19}	11.1	1.3
Sample D	1085	1.7×10^3	9.3×10^{19}	39.7	7.0
Sample E	3617	1.3×10^3	1.1×10^{20}	45.0	6.4

that crystal symmetry is lifted for GaN layers with high Si doping having a carrier concentration $\geq 9.5 \times 10^{19}\text{ cm}^{-3}$.

Additionally, the increase of Si doping results in a strong broadening (already visible at a carrier concentration of $2.5 \times 10^{19}\text{ cm}^{-3}$) and disappearance of the $A_1(\text{LO})$ Raman peak at 735 cm^{-1} , which is allowed in a perfect $Z//[001]$ GaN single crystal and $Z(X-\bar{Y})\bar{Z}$ Raman configuration.^{38,39} The $E_1(\text{LO})$ Raman peak at 743 cm^{-1} becomes visible for carrier concentrations $\geq 9.5 \times 10^{19}\text{ cm}^{-3}$. The $E_1(\text{LO})$ phonon mode is allowed only in the $X(Y-\bar{Y})$ Raman configuration, this is again ascribed to crystal symmetry lifting induced by the high Si doping concentration.

On the other hand, the GaN $E_2^{(2)}$ phonon mode is present for every carrier concentration. A more detailed analysis of its spectral position and FWHM is summarized in Fig. 12, where the results are averaged over the 10 different measurement points (line scan) for each GaN sample.

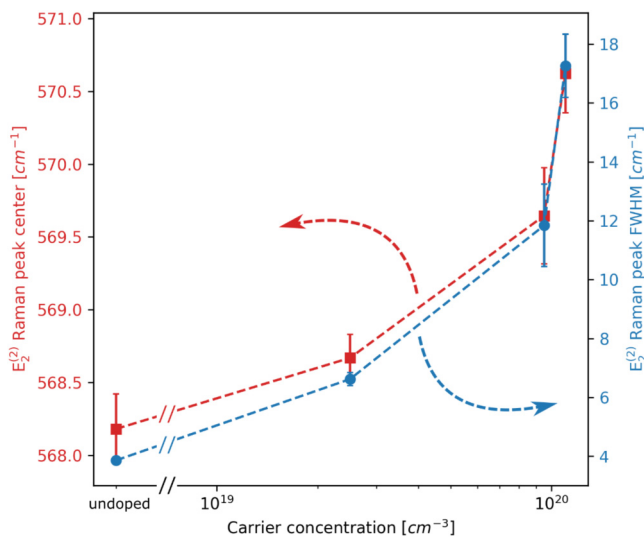


FIG. 12. Spectral position of the $E_2^{(2)}$ Raman peak center (red squares) and $E_2^{(2)}$ Raman peak FWHM (blue circles) of GaN layers with different carrier concentration: undoped (sample A), $2.5 \times 10^{19}\text{ cm}^{-3}$ (sample C), $9.5 \times 10^{19}\text{ cm}^{-3}$ (sample D), and $1.1 \times 10^{20}\text{ cm}^{-3}$ (sample E). The average and standard deviation error are evaluated over 10 points in a line scan. The colored arrows point toward the corresponding y axis. This figure's color version is available online.

Figure 12 displays the spectral position of the $E_2^{(2)}$ GaN Raman peak center (red squares) as a function of the carrier concentration. The undoped GaN sample (A) has a $E_2^{(2)}$ Raman peak centered at 568.1 cm^{-1} , and its spectral position increases monotonically with the Si doping reaching 570.5 cm^{-1} for a carrier concentration of $1.1 \times 10^{20}\text{ cm}^{-3}$ (sample E). The $E_2^{(2)}$ Raman peak position of the undoped GaN sample A corresponds almost with that of strain-free bulk GaN: 568 cm^{-1} (Ref. 37), while the $E_2^{(2)}$ Raman peak of sample E, centered at 570.5 cm^{-1} (carrier concentration of $1.1 \times 10^{20}\text{ cm}^{-3}$), is ascribed to an in-plane compressive stress of about 0.3 GPa (Ref. 37). The stress increase with Si doping is assumed to be due to the GaN lattice deformation caused by an increase of incorporated Si impurities.

Additionally, Fig. 12 indicates that the FWHM of the $E_2^{(2)}$ Raman peak (blue points) increases monotonically from 4 cm^{-1} for the undoped GaN, up to 17 cm^{-1} for the highly doped GaN layer with a carrier concentration of $1.1 \times 10^{20}\text{ cm}^{-3}$. This result is a clear indication that the incorporation of a large amount of Si impurities has a detrimental effect on the GaN crystal order.

The light-emitting properties of the GaN layers with different amounts of Si doping were also investigated by photoluminescence,

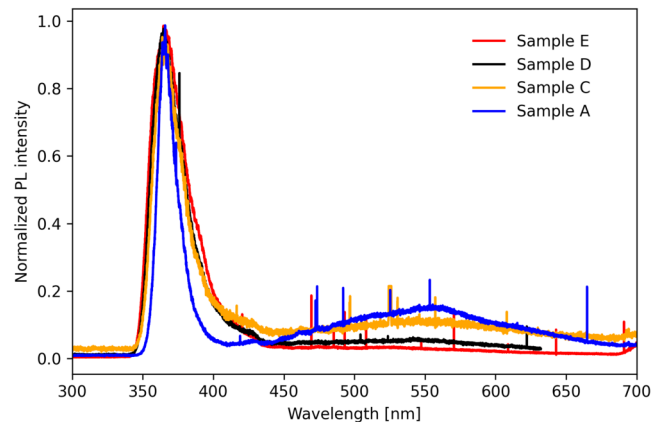


FIG. 13. Photoluminescence spectra of undoped (blue—sample A), Si doped with carrier concentration $2.5 \times 10^{19}\text{ cm}^{-3}$ (orange—sample C), $9.5 \times 10^{19}\text{ cm}^{-3}$ (black—sample D), and sample E $1.1 \times 10^{20}\text{ cm}^{-3}$ (red—sample E) GaN layers. The sharp spikes in the PL intensity are due to cosmic rays hitting the CCD detector. This figure's color version is available online.

and the results are reported in Fig. 13. Here, the intensity-normalized PL spectra show two main spectral features: (1) the intense near-bandgap PL emission around 364 nm (present for all investigated samples) and (2) weaker and broader defect-related emission around 550 nm. Similar to the Raman spectra for the $E_2^{(2)}$ phonon mode, the FWHM of near-bandgap PL emission around 364 nm changes from a minimum of 16 nm for the undoped sample A, to a maximum of 30 nm for the highest dopant concentration sample E.⁴⁰ The doping-induced broadening agrees with previously reported data and can be ascribed to local potential fluctuation caused by a random distribution of Si impurities.⁴¹

The intensity of the defect-related PL peak centered at 550 nm⁴² decreases with increasing the carrier concentration and Si doping level. Indeed, substitutional Si dopants progressively quench the yellow radiative recombination associated with defects, in agreement with earlier results on Si-doped GaN.⁴³

IV. CONCLUSION

In this work, we have shown that highly c axis oriented GaN thin films can be grown on sapphire (0001) by reactive sputter deposition from a liquid Ga target using Ar/N₂ gas mixtures in an industrial production system designed for 6 in. substrates. Films grown without any doping exhibit a high electrical resistance above 800 kΩ/sq. To demonstrate the ability of the presented technique to prepare films with variable electrical conductivity, GaN films were doped with Si during deposition. The lowest resistivity values obtained are 1300 μΩ cm. Hall measurements are used to determine the carrier concentration and carrier mobility. The doping levels are characterized by LA-ICP-MS and compared to the carrier concentration, which amounts for the highest doped layer to $1.1 \times 10^{20} \text{ cm}^{-3}$ with a carrier mobility of $45 \text{ cm}^2 \text{ V}^{-1} \text{ s}^{-1}$. Despite the high doping levels, a high degree of crystal orientation is attained, as evidenced by the FWHM < 0.3° of the XRD rocking curves for low doped layers and < 0.5° for the highest doping levels.

The film morphology shows faceted surfaces for low doping levels, while at higher doping levels of 10^{20} cm^{-3} , flat surfaces are attained. The faceted growth causes compressive in-plane stresses of ca. 0.27 GPa, which is absent in both undoped and highly doped samples. A progressive deterioration of the crystalline quality with increasing doping levels is deduced from Raman investigations. The peak shift of the $E_2^{(2)}$ Raman mode indicates strained layers due to doping with an in-plane compressive stress of about 0.3 GPa, which is in excellent agreement with the values obtained from XRD. The 2θ peak shifts from the bulk value and is calculated to an out-of-plane stress of −0.77 GPa and in-plane stress of 0.352 GPa.

This work shows that reactive sputter deposition from a liquid Ga target is a viable alternative to conventional preparation methods for GaN films. Due to the low resistivity, functional devices may be fabricated on 6 in. substrates by doping during sputter deposition. Additional studies with a more flexible dopant source such as cosputtering or gaseous doping precursors are expected to lead to improved results with higher carrier mobilities and reduced resistivities on large area GaN films. This will also enable experiments with different dopants such as germanium or

magnesium or enable layers alloyed with aluminum and/or indium.

ACKNOWLEDGMENTS

The authors thank the research group of Wegscheider (ETH Zürich) for use of their Hall measurement equipment. They also acknowledge the support of the Scientific Center for Optical and Electron Microscopy ScopeM of the Swiss Federal Institute of Technology ETHZ for the SEM measurements and access to the Raman facility. J.P., E.B., and F.P. acknowledge the University of Milano Bicocca for the funding Bando Infrastrutture di Ricerca 2021. J.P. acknowledges financial support from FSE REACT-EU (grant 2021-RTDAPON-144).

AUTHOR DECLARATIONS

Conflict of Interest

D. Jaeger and T. Tschirky are coauthors of a patent submission WO2020083882A1, which is quoted as Ref. 25.

Author Contributions

Patrick Loretz: Investigation (equal). **Thomas Tschirky:** Formal analysis (equal). **Fabio Isa:** Investigation (equal). **Jörg Patscheider:** Supervision (equal). **Matthias Trottmann:** Investigation (equal). **Adrian Wichser:** Investigation (equal). **Jacopo Pedrini:** Investigation (equal). **Emiliano Bonera:** Investigation (equal). **Fabio Pezzoli:** Investigation (equal). **Dominik Jaeger:** Conceptualization (equal); Funding acquisition (equal).

DATA AVAILABILITY

The data that support the findings of this study are available from the corresponding author upon reasonable request.

REFERENCES

- O. Ambacher, *J. Phys. Appl. Phys.* **31**, 2653 (1998).
- S. P. DenBaars *et al.*, *Acta Mater.* **61**, 945 (2013).
- T. D. Moustakas and R. Paiella, *Rep. Prog. Phys.* **80**, 106501 (2017).
- A. Khaligh and S. Dusmez, *IEEE Trans. Veh. Technol.* **61**, 3475 (2012).
- U. K. Mishra, S. Likun, T. E. Kazior, and Y.-F. Wu, *Proc. IEEE* **96**, 287 (2008).
- B. Wu, see <http://www.ledinside.com/node/31987> for “PlayNitride Introduces New MicroLED Display Prototypes at SID Displayweek 2021,” LEDinside (21 May 2021).
- C. Zhang, R. ElAfandy, and J. Han, *Appl. Sci.* **9**, 1593 (2019).
- S. N. Alam, V. Z. Zubialevich, B. Ghafary, and P. J. Parbrook, *Sci. Rep.* **10**, 16205 (2020).
- I. Akasaki and H. Amano, *Jpn. J. Appl. Phys.* **45**, 9001 (2006).
- P. Mukish, M. Verstraete, P. Boulay, and J. Thomé, see www.yole.fr/Iso_upload/news/2020/PR_UV_LED_MarketUpdate_YOLEGROUP_Oct2020.Pdf for “UV LEDs: One Solution to Contain the COVID-19 Pandemic,” 15 October 2020 (2021).
- H. Lahrèche, M. Leroux, M. Laügt, M. Vaille, B. Beaumont, and P. Gibart, *J. Appl. Phys.* **87**, 577 (2000).
- S. Nakamura, *Jpn. J. Appl. Phys.* **30**, L1705 (1991).
- H. Tang and J. B. Webb, *Appl. Phys. Lett.* **74**, 2373 (1999).
- K. Fujito, S. Kubo, H. Nagaoka, T. Mochizuki, H. Namita, and S. Nagao, *J. Crystal Growth*, **311**, 3011 (2009).

- ¹⁵See <https://www.universitywafer.com/bulk-gan.html> for “Bulk Gallium Nitride (GaN) Direct Wide Bandgap Semiconductor,” 1 October 2018 (2021).
- ¹⁶S. Hagedorn, T. Khan, C. Netzel, C. Hartmann, S. Walde, and M. Weyers, *Phys. Status Solidi A* **217**, 2000473 (2020).
- ¹⁷H. Miyake, C.-H. Lin, K. Tokoro, and K. Hiramatsu, *J. Cryst. Growth* **456**, 155 (2016).
- ¹⁸H. Shinoda and N. Mutsukura, *Vacuum* **138**, 87 (2017).
- ¹⁹K. Ueno, F. Taiga, A. Kobayashi, and H. Fujioka, *Sci. Rep.* **9**, 20242 (2019).
- ²⁰M. Junaid, C.-L. Hsiao, J. Palisaitis, J. Jensen, P. O. Å. Persson, L. Hultman, and J. Birch, *Appl. Phys. Lett.* **98**, 141915 (2011).
- ²¹M. Junaid, *Magnetron Sputter Epitaxy of GaN* (Department of Physics, Chemistry and Biology, Linköping University, Linköping, Sweden, 2011).
- ²²C. M. Furqan, J. Y. L. Ho, and H. S. Kwok, *Surf. Interfaces* **26**, 101364 (2021).
- ²³Y. Arakawa, K. Ueno, H. Imabeppu, A. Kobayashi, J. Ohta, and H. Fujioka, *Appl. Phys. Lett.* **110**, 042103 (2017).
- ²⁴See www.evatecnet.com/products/clusterline-family/clusterline-200/ for “CLUSTERLINE® 200” (2021).
- ²⁵D. Jaeger, T. Tschirky, M. Rechsteiner, H. Felzer, and H. Rohrmann, PCT Publication No. WO2020083882A1 (30 April 2020).
- ²⁶T. Metzger *et al.*, *Philos. Mag. A* **77**, 1013 (1998).
- ²⁷N. G. Weimann, L. F. Eastman, D. Doppalapudi, H. M. Ng, and T. D. Moustakas, *J. Appl. Phys.* **83**, 3656 (1998).
- ²⁸F. Kaess *et al.*, *J. Appl. Phys.* **120**, 235705 (2016).
- ²⁹N. A. K. Kaufmann, L. Lahourcade, B. Hourahine, D. Martin, and N. Grandjean, *J. Cryst. Growth* **433**, 36 (2016).
- ³⁰G. Mula, B. Daudin, C. Adelmann, and P. Peyla, *MRS Internet J. Nitride Semicond. Res.* **5**, 202 (2000).
- ³¹Y. Daigo and N. Mutsukura, *Thin Solid Films* **483**, 38 (2005).
- ³²M. Junaid, P. Sandström, J. Palisaitis, V. Darakchieva, C.-L. Hsiao, P. O. Å. Persson, L. Hultman, and J. Birch, *J. Phys. Appl. Phys.* **47**, 145301 (2014).
- ³³*Handbook of GaN Semiconductor Materials and Devices*, edited by W. Bi, H.-C. Kuo, P.-C. Ku, and B. Shen (CRC, Boca Raton, 2017).
- ³⁴M. A. Moram and M. E. Vickers, *Rep. Prog. Phys.* **72**, 036502 (2009).
- ³⁵B. Heying, X. H. Wu, S. Keller, Y. Li, D. Kapolnek, B. P. Keller, S. P. DenBaars, and J. S. Speck, *Appl. Phys. Lett.* **68**, 643 (1996).
- ³⁶H. Harima, *J. Phys.: Condens. Matter* **14**, R967 (2002).
- ³⁷I.-H. Lee, I.-H. Choi, C.-R. Lee, E. Shin, D. Kim, S. K. Noh, S.-J. Son, K. Y. Lim, and H. Jae Lee, *J. Appl. Phys.* **83**, 5787 (1998).
- ³⁸S. Tripathy, S. J. Chua, P. Chen, and Z. L. Miao, *J. Appl. Phys.* **92**, 3503 (2002).
- ³⁹V. Yu. Davydov, N. S. Averkiev, I. N. Goncharuk, D. K. Nelson, I. P. Nikitina, A. S. Polkovnikov, A. N. Smirnov, M. A. Jacobson, and O. K. Semchinova, *J. Appl. Phys.* **82**, 5097 (1997).
- ⁴⁰E. F. Schubert, I. D. Goepfert, W. Grieshaber, and J. M. Redwing, *Appl. Phys. Lett.* **71**, 921 (1997).
- ⁴¹I.-H. Lee, J. J. Lee, P. Kung, F. J. Sanchez, and M. Razeghi, *Appl. Phys. Lett.* **74**, 102 (1999).
- ⁴²M. A. Reshchikov and H. Morkoç, *J. Appl. Phys.* **97**, 061301 (2005).
- ⁴³H. C. Yang, T. Y. Lin, and Y. F. Chen, *Phys. Rev. B* **62**, 12593 (2000).